Nuclear Instruments and Methods in Physics Research A 703 (2013) 38–44

Contents lists available at SciVerse ScienceDirect

Nuclear Instruments and Methods in Physics Research A

journal homepage: www.elsevier.com/locate/nima

Development of a front-end analog circuit for multi-channel SiPM readout and performance verification for various PET detector designs

Guen Bae Ko [a,b,f], Hyun Suk Yoon [a,b,f], Sun Il Kwon [a,e,f], Chan Mi Lee [a,b,f], Mikiko Ito [a,f], Seong Jong Hong [g], Dong Soo Lee [a,c,e,f], Jae Sung Lee [a,b,d,e,f,*]

[a] Department of Nuclear Medicine, Seoul National University, 103 Daehak-ro, Jongro-gu, Seoul 110-799, Republic of Korea
[b] Department of Biomedical Sciences, Seoul National University, 103 Daehak-ro, Jongro-gu, Seoul 110-799, Republic of Korea
[c] WCU Molecular Medicine and Biopharmaceutical Sciences, Seoul National University, 599 Gwanak-ro, Gwanak-gu, Seoul 151-742, Republic of Korea
[d] WCU Brain and Cognitive Sciences, Seoul National University, 599 Gwanak-ro, Gwanak-gu, Seoul 151-747, Republic of Korea
[e] Interdisciplinary Program in Radiation Applied Life Science, Seoul National University, 103 Daehak-ro, Jongro-gu, Seoul 110-799, Republic of Korea
[f] Institute of Radiation Medicine, Medical Research Center, Seoul National University, 103 Daehak-ro, Jongro-gu, Seoul 110-799, Republic of Korea
[g] Department of Radiological Science, Eulji University, 212 Yangji-dong, Sujeong-gu, Seongnam-si, Gyeonggi-do, 461-713, Republic of Korea

ARTICLE INFO

Article history:
Received 14 June 2012
Received in revised form
8 November 2012
Accepted 15 November 2012
Available online 23 November 2012

Keywords:
Positron emission tomography (PET)
Silicon photomultiplier (SiPM)
Geiger-mode APD (GAPD)
PET/MRI scintillation detector

ABSTRACT

Silicon photomultipliers (SiPMs) are outstanding photosensors for the development of compact imaging devices and hybrid imaging systems such as positron emission tomography (PET)/ magnetic resonance (MR) scanners because of their small size and MR compatibility. The wide use of this sensor for various types of scintillation detector modules is being accelerated by recent developments in tileable multichannel SiPM arrays. In this work, we present the development of a front-end readout module for multi-channel SiPMs. This readout module is easily extendable to yield a wider detection area by the use of a resistive charge division network (RCN). We applied this readout module to various PET detectors designed for use in small animal PET/MR, optical fiber PET/MR, and double layer depth of interaction (DOI) PET. The basic characteristics of these detector modules were also investigated. The results demonstrate that the PET block detectors developed using the readout module and tileable multi-channel SiPMs had reasonable performance.

1. Introduction

Silicon photomultipliers (SiPM) is regarded as a promising device in many photon counting applications including high-energy physics, astroparticle physics, and medical imaging [1–3]. In nuclear medicine, recent studies have shown that SiPMs are suitable photon counting devices for time-of-flight (TOF) positron emission tomography (PET) [4–6] and hybrid PET/MR (magnetic resonance) imaging [7–14] because of their fast response time and insensitivity to magnetic fields, respectively [3,15]. The compact size of SiPMs is also useful in the development of PET detector modules for small animal imaging and depth-of-interaction (DOI) measurement [2,16–19].

Several groups including our own have shown that SiPMs are suitable for signal readout schemes using block detectors in PET [13,16,20]. In these studies, to construct block detectors, a number of single-channel SiPMs were arranged in a rectangular array with relatively large dead space. Special frames or materials required for fixing them are troublesome in the construction of arrays and extension of the detection area. On the contrary, the recent development of tileable multi-channel SiPMs enables the easy construction of block detectors. Moreover, the multi-channel SiPMs have a relatively small dead space between each channel, facilitating the use of thinner light guides for spreading scintillation photons. Thus, the block detectors constructed using tileable multi-channel SiPMs would have better energy and timing resolution than the single-channel design because the light loss due to dead space is much smaller in multi-channel SiPM detectors.

Therefore, we employed these multi-channel SiPMs for the development of MR-compatible PET block detectors with and without the use of short optical fibers between scintillation crystals and SiPMs [10,11]. In our recent works, we applied the same front-end readout modules for multi-channel SiPMs although the numbers of SiPM channels were different in each detector configuration. In this work, we therefore present the detailed design scheme of this front-end readout module based on the charge division network that was employed for the easy extension of the module to a wider detection area. The detector configuration and physical performance of

* Corresponding author at: Department of Nuclear Medicine, Seoul National University College of Medicine, 28 Yungun-Dong, Chongno-Gu, Seoul 110-744, Republic of Korea. Tel.: +82 2 2072 2938; fax: +82 2 745 2938.
E-mail address: jaes@snu.ac.kr (J.S. Lee).

0168-9002/$ - see front matter © 2012 Elsevier B.V. All rights reserved.
http://dx.doi.org/10.1016/j.nima.2012.11.087

various detectors developed for small animal PET/MR [10], optical fiber PET/MR [11], and double layer depth of interaction (DOI) PET using this front-end readout module will be presented.

2. Materials and methods

2.1. Silicon photomultiplier

The characteristics of the tileable multi-channel SiPMs (S11064 series; Hamamatsu, Japan) with 4×4 channels are listed in Table 1. The S11064-050P SiPM has 400 microcells per mm^2 and a relatively high fill factor in comparison with S11064-025P. Because photon detection efficiency (PDE) is determined by the quantum efficiency (QE), avalanche probability, and fill factor, the relatively high fill factor leads to high PDE. The only drawback is worse energy linearity due to the limited number of microcells. In PET applications, however, the total microcell number of S11064-050P (3,600) is sufficient for the combination of 511 keV gamma rays and the LGSO or LYSO crystals used in this study [21].

Table 1
Main parameters of the multi-channel SiPM (HAMAMATSU S11064).

Parameter	Hamamatsu S11064 Series	
	S11064-025 P	S11064-050 P
Number of channels	16 (4 × 4)	
Effective active area/channels (mm)	3 × 3	
No. of pixels/channels	14400	3600
Pixel size (μm)	25 × 25	50 × 50
Fill factor (%)	30.8	61.5
Dark count/channel (Mcps)	4	6
Terminal capacitance/channel (pF)	320	
Gain	2.75×10^5	7.5×10^5

2.2. Electronics for signal multiplexing and data acquisition

We designed the SiPM front-end readout module with which the four tileable 4×4 channel SiPMs can be combined (Fig. 1). This means that the detector module needs at least 64 signal lines for a single signal readout scheme or 128 signal lines for a differential signal readout scheme if no signal multiplexing is involved. In this situation, a very sophisticated and complicated system (i.e. ASIC) is necessary to process this large number of signals individually. Furthermore, the large number of signal lines has some potential risk in simultaneous PET/MR applications because it would require very careful shielding for the large number of signal cables to reduce RF interference between PET and MRI. Therefore, we multiplexed the signals from the 64 SiPM channels to four position encoding signals (A, B, C, and D) using a resistive charge division network (RCN) [22] (Fig. 1(b)). From the encoding signals, X and Y positions were decoded according to the following equations:

$$X = \frac{(A+D)-(B+C)}{A+B+C+D} \tag{1}$$

$$Y = \frac{(A+B)-(C+D)}{A+B+C+D} \tag{2}$$

The multiplexed position signals (A–D) were amplified by a factor of 10–20 with high-speed differential amplifier (AD8132; Analog Devices, USA). The signal to extract energy and timing information (called the sum signal; S) was generated by adding four multiplexed position signals using a differential summing amplifier. A differential signaling scheme was especially useful for reducing RF noise or interference for specific purposes, including the MR-compatible PET. Fig. 1 shows the SiPM bias schematics, RCN, and amplifier circuits.

This front-end readout module based on RCN makes the PET block detector easily extendable without requiring a change of DAQ system

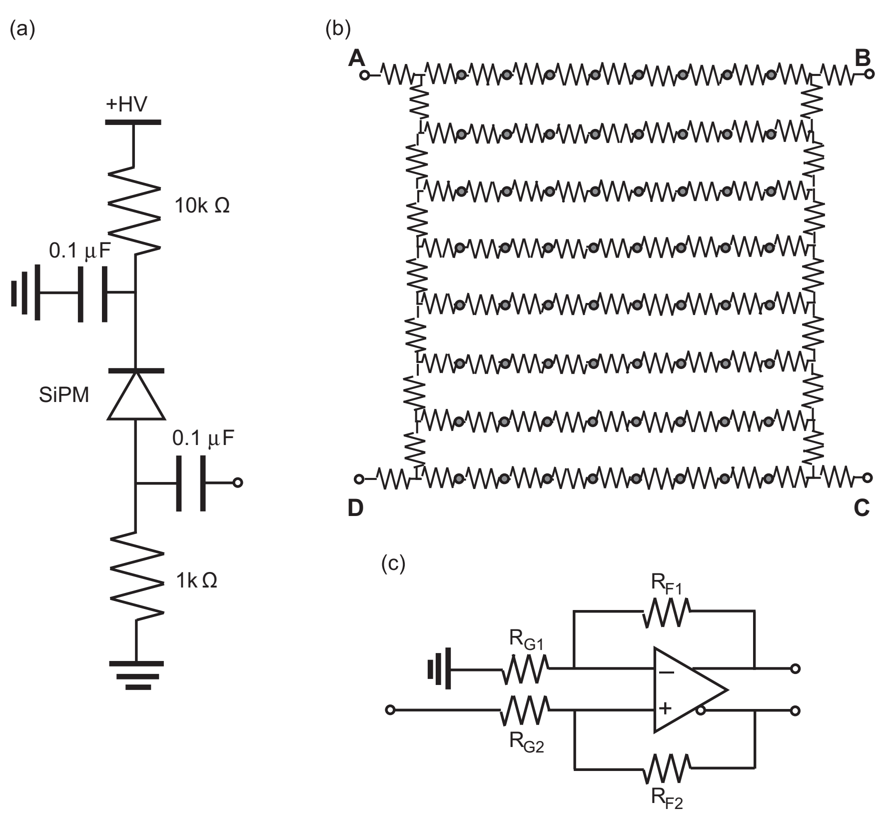

Fig. 1. Schematic of the front-end analog circuit for the SiPM readout module. (a) SiPM biasing circuit. (b) Resistive charge division network (RCN). (c) Differential amplifier circuit.

because the number of signal lines is always the same regardless of the number of SiPMs connected to the detector module.

To verify whether this front-end readout module was suitable for SiPMs, electric circuit simulation was performed using PSpice (Cadence, USA). This simulation was only for SiPM cells and analog front-end circuits without consideration of scintillation, light loss and other effects because the linearity of X and Y positions are mainly determined by these two components. SiPM cells were modeled as combinations of resistors, capacitors, switches, and current sources [23,24]. By this simulation, the resistor values of the RCN circuit were carefully determined to match the input impedance from each of the SiPM channels. Fig. 2(a) shows the output pulses measured at positions A–D when only the SiPM cell nearest to A was fired. The SiPM cell positions were successfully separated using these four multiplexed position signals as illustrated in Fig. 2(b).

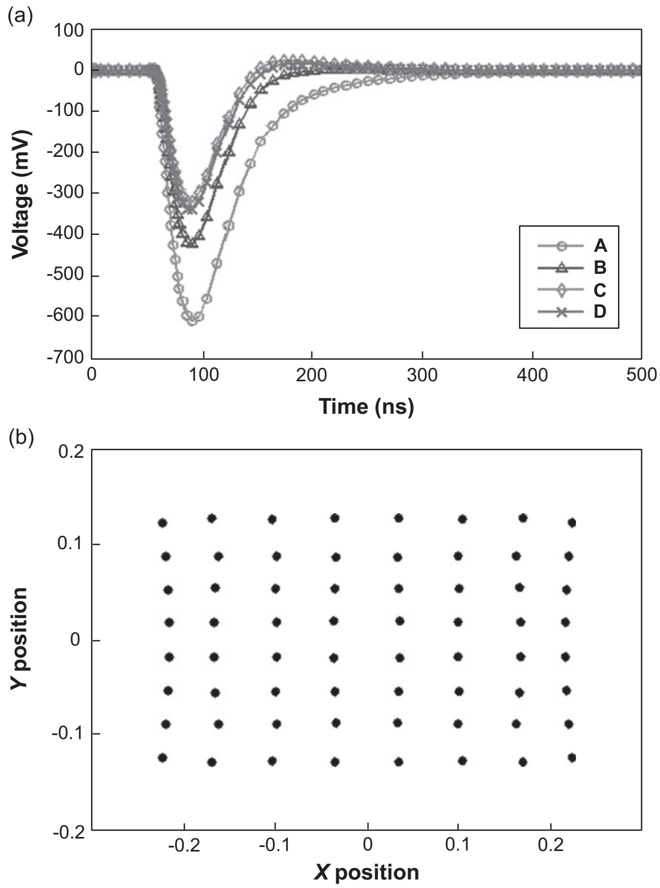

Fig. 2. Electrical stimulation results of the SiPM block detector. (a) Output pulses measured at positions A–D when only the SiPM cell nearest to A was fired. (b) Position map of 64 channels obtained using the decoding scheme shown in Eqs. (1) and (2).

A digital temperature sensor (TCN75; Microchip, USA) was attached next to the SiPMs to monitor the operating temperature. Because photon detection performance of SiPMs, such as internal amplification gain and dark count rate, is sensitive to temperature change, temperature monitoring is essential for bias voltage control in a SiPM-based PET system. This sensor has a precision of 0.5 °C and can be read out via an I^2C bus.

Data were acquired using a FPGA-based DAQ system [10]. In the FPGA-based DAQ system, using the discriminator signal of the sum signal, our custom-built FPGA-based coincidence detector identifies the coincidence events and makes trigger signals of ADCs that are matched coincidence pairs [25]. The multiplexed position signals were sampled at 170 MSPS with 12 bit resolution [10]. The crystal position, energy, and coincidence pair were calculated in real time and transmitted to a PC. In addition, pulse shape analysis for depth of interaction (DOI) measurement is also possible in the FPGA-based DAQ system. To acquire timing performance information, we measure the time difference between the discriminator signal of each detector's sum signal and the coincidence signal using VERSAModule Eurocard (VME) standard TDC module (V775N; Caen, Italy).

2.3. Single-layer LGSO PET detector

2.3.1. Detector configuration.

A detector module using a $L_{0.95}$GSO ($Lu_{1.9}Gd_{0.1}SiO_4$:Ce; Hitachi Chemical, Japan) crystal and readout module with four (2×2 array) S11064-050 P SiPMs was produced (mainly for small animal PET/MRI research). The 64 cells of the SiPMs were connected with a

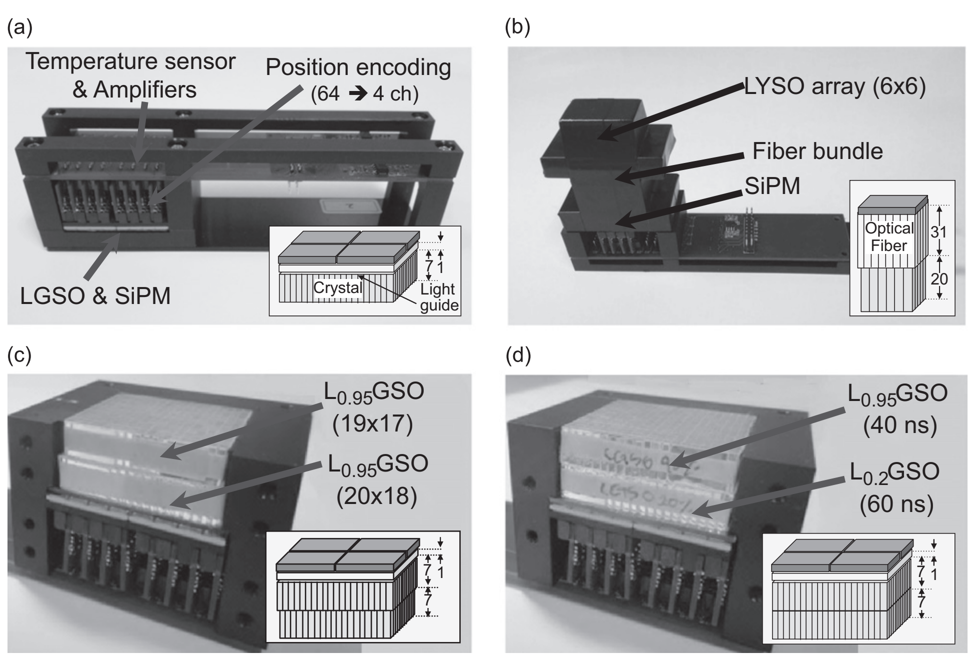

Fig. 3. PET block detectors developed using the SiPM readout module, multi-channel SiPMs, and LGSO crystal arrays. (a) Single-layer LGSO block detector. (b) Short optical fiber PET detector. (c) DOI PET detector using the relative offset method. (d) DOI PET detector using pulse shape discrimination.

20×18 $L_{0.95}GSO$ crystal array. The dimensions of each $L_{0.95}GSO$ pixel were $1.5 \times 1.5 \times 7$ mm^3 and the crystal pitch was 1.62 mm due to the ESR reflector (3 M, USA) between pixels. A light guide with 1 mm thickness made by soft polyvinyl chloride (PVC) was inserted between the crystal array and SiPMs to spread scintillation light. Optical grease (BC-630; Oken, Japan) was used for the coupling of the $L_{0.95}GSO$ crystal, light guide, and SiPMs. Fig. 3(a) shows the single-layer PET block detector that consists of four SiPMs with the $L_{0.95}GSO$ crystal block.

2.3.2. Performance evaluation.

Energy resolution, coincidence resolving time, crystal map, and intrinsic spatial resolution were obtained for performance verification of the detector module. The crystal maps were acquired by irradiating the block detector with a 107 kBq (2.89 μCi) ^{22}Na point source located about 20 cm away from the detector surface with coincidence triggering. The total valid event count was approximately 3.5 M to clearly resolve all the crystals. Energy spectra of individual crystals were estimated from the crystal map and average energy resolution was calculated after peak alignment.

Coincidence resolving time was measured against a LYSO ($4 \times 4 \times 10$ mm^3)-fast photomultiplier tube (R9800; Hamamatsu, Japan) reference detector that has 198 ps timing resolution [26]. The coincidence counts of two detectors were plotted as a detecting time difference. From the plot (similar to Fig. 5), we obtained the coincidence resolving time as the full width at half maximum (FWHM) of the time delay's distribution. To measure intrinsic spatial resolution, two single-layer LGSO PET detectors were located facing each other with a distance of 9.0 cm. The ^{22}Na point source (nominal diameter, 0.25 mm) was moved in the transverse direction with a step size of 0.2 mm from the center to the edge of the two detectors. At each location, data were acquired for 5 min. From the data, the coincidence counts between the exactly opposed crystal pairs were plotted as a function of the source position. The FWHM of the count distribution at each crystal pair determines the intrinsic spatial resolution of the detector.

2.4. Double-layer DOI PET detector

2.4.1. Relative offset method.

We also tested the feasibility of DOI PET detectors based on the multi-channel SiPMs. We constructed two different double-layer DOI scintillator blocks as illustrated in Fig. 3(c) and (d). One of the blocks is based on the relative offset method [27,28]. The double-layer DOI detector was constructed from a 19×17 $L_{0.95}GSO$ crystal array on a 20×18 $L_{0.95}GSO$ crystal array. The dimensions of each LGSO pixel are also $1.5 \times 1.5 \times 7$ mm^3. The upper 19×17 array was placed on the lower 20×18 array with a shift of half the element pitch ($\sim$0.81 mm) in both the X and Y directions. To obtain the crystal maps for the verification of this method, a ^{22}Na point source was used to irradiate the front of the crystal arrays.

2.4.2. Pulse shape discrimination.

The other DOI scheme is pulse shape discrimination (PSD) [29]. A phoswich-type double-layer detector was constructed with two types of LGSO crystal that had different levels of lutetium content. The upper 20×18 $L_{0.95}GSO$ crystal array was located on a lower 20×18 $L_{0.2}GSO$ ($Lu_{0.4}Gd_{1.6}SiO_4$:Ce) array. The layer of interaction was distinguished by the ratios of tail integration to full integration of the scintillation pulse [30] because they have different decay times ($\tau = 40$ ns for $L_{0.95}GSO$ and 60 ns for $L_{0.2}GSO$). To obtain the pulse property of each detector, the detector was irradiated with a ^{22}Na point source from the side of the crystal array. The radiation beam was collimated by a pair of lead blocks to irradiate each layer differently. From the acquired data, we plotted the ratios of tail integration to full integration (energy) of the scintillation pulse for each layer. We chose a threshold value that was the overlap point of the two graphs. For the each layer, the accuracy of the correct interaction layer was calculated from the ratio of the counts above or below the threshold to the total count. In the FPGA-based DAQ system mentioned Section 2.2, the tail to full integration ratio was calculated and compared to set the threshold in real time.

We obtained 10,000 sample scintillation pulses for each layer to assess the depth identification accuracy.

2.5. Short optical fiber PET detector

The detector scheme was also applied to a short optical fiber PET detector. This detector concept was proposed to improve RF transmission using a body coil in PET/MR applications [8,11]. The detector consists of 6×6 LYSO (SIPAT, China) crystals and 310 optical fibers (Kuraray, Japan) of 1.0 mm diameter. The dimensions of each LYSO pixel were $2.47 \times 2.74 \times 20$ mm^3 and the length of the optical fibers was 31 mm. For this detector structure, only one SiPM was connected to the detector circuit, instead of the usual four SiPMs. Using the front-end readout module, the feasibility and performance of the concept of scintillation light transfer to SiPMs using short optical fibers was verified.

Fig. 3(b) shows the short optical fiber PET detector. Crystal map and energy spectra were acquired to verify the feasibility of short optical fiber PET detectors. The average energy resolution was also calculated.

3. Results

3.1. Single-layer LGSO PET detector

The crystal map of a 20×18 $L_{0.95}GSO$ crystal array and energy spectra for individual $L_{0.95}GSO$ crystals are shown in Fig. 4. We obtained $13.6 \pm 0.71\%$ average energy resolution for single crystals (maximum = 15.1%, minimum = 11.5%). All of the 1.5 mm crystal was clearly resolved in the crystal map including the peripheral regions of the crystal array. The average peak-to-valley ratio for the row and column of crystals was 3.56 and 3.65 respectively. This result indicates that a 1 mm thick soft PVC light guide was suitable for this type of SiPM block detector scheme.

The measured coincidence resolving time with a fast reference detector (198 ps timing resolution) was 1.225 ns in the center and 0.774 ns in the corner of the block detector at 22 °C (Fig. 5). Fig. 6 shows the intrinsic resolution profile of this SiPM detector. The average intrinsic spatial resolution was 1.45 mm for a 1.62 mm crystal pitch.

3.2. Dual-layer DOI PET detectors

Fig. 7 illustrates the separation of the two layers in each of the dual layer DOI PET detectors. For the relative offset method, the two crystal layers were well separated in the crystal map (Fig. 7(a)).

For the pulse shape discrimination method, the spectra of the tail/full integration ratio were different between the $L_{0.95}GSO$ and $L_{0.2}GSO$ layers as shown in Fig. 7(b). Using the thresholds with the highest reliability, 91.0% of the $L_{0.95}GSO$ pulses and 92.1% of $L_{0.2}GSO$ pulses were detected correctly.

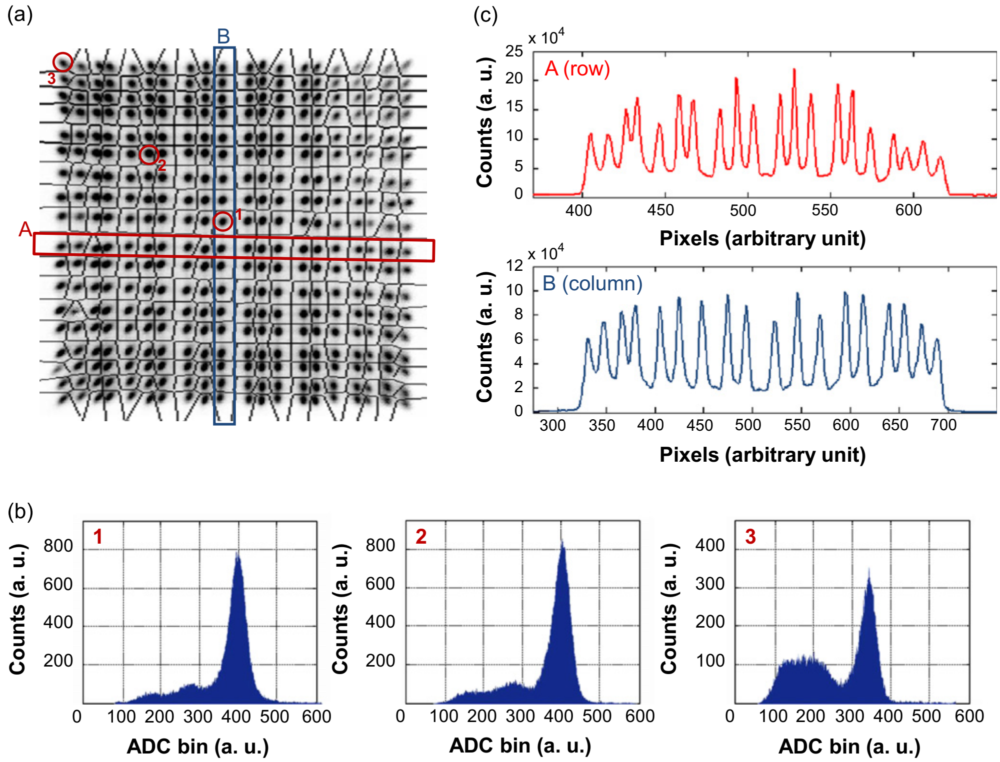

Fig. 4. Flood map of single-layer LGSO block detector. (a) Flood map with fishnet. (b) Energy spectra for individual crystals located at position 1 (energy resolution = 13.08%), 2 (13.19%), and 3 (13.53%). (c) Profiles for row A and column B.

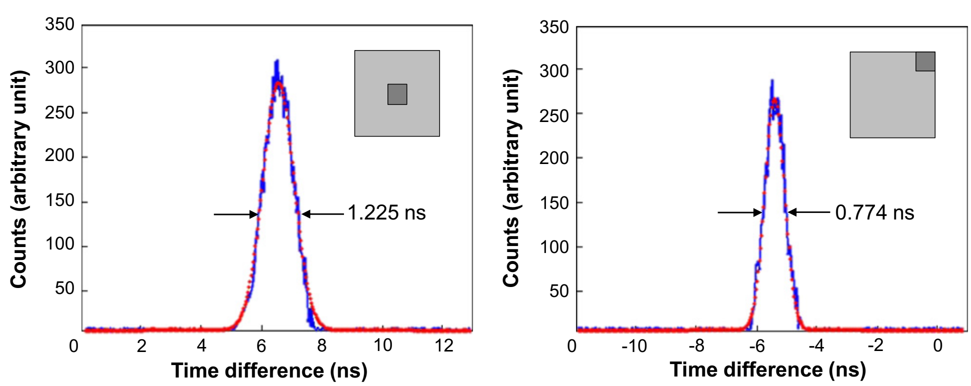

Fig. 5. Timing spectrum of single-layer LGSO block detector measured against a LYSO-fast photomultiplier tube (Hamamatsu R9800). The coincidence resolving time at 22 °C measured 1.225 ns in the center and 0.774 ns in the corner.

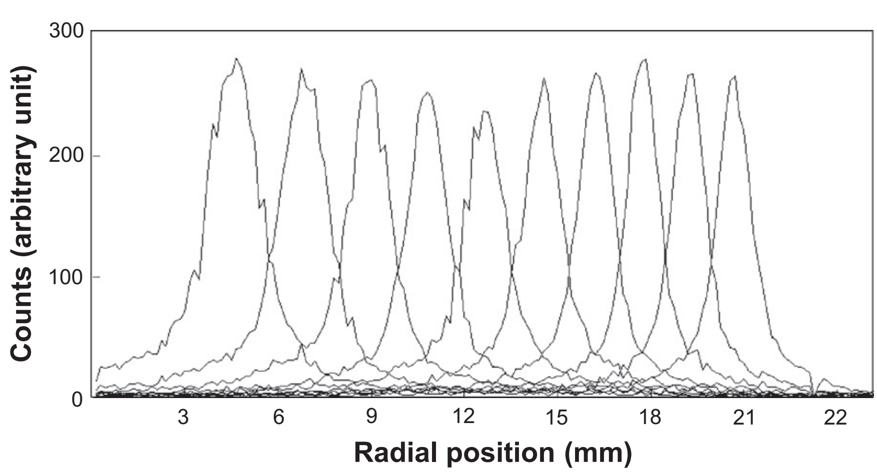

Fig. 6. Intrinsic resolution profile of single-layer LGSO block detector. Average, best and worst intrinsic resolutions were 1.45 mm, 1.30 mm, and 1.55 mm, respectively. Each profile shows the count distribution versus crystal position for each different source position.

3.3. Short optical fiber PET detector

Fig. 8 shows a crystal map and energy spectra of 36 crystals from a short optical fiber PET detector. The crystals were successfully resolved in the crystal map. The average energy resolution of 36 crystals was $25.6 \pm 1.11\%$.

4. Discussions and conclusion

The aim of this study was to develop a multi-purpose extendable PET detector module using multi-channel SiPMs and to evaluate its physical characteristics for various PET detector designs, such as single-layer LGSO PET detectors, 2-layer DOI detectors, and short optical fiber detectors.

For a single-layer LGSO PET detector, the energy resolution for individual crystals was 13.6% on average. In previous studies using single-type SiPMs combined with the light and charge sharing signal readout method, the average energy resolutions of the block detectors were 25.8% with a $1.5 \times 1.5 \times 7\ \text{mm}^3$ crystal [16], 22.0% with a $1.5 \times 1.5 \times 10\ \text{mm}^3$ crystal [13], and 20.0% with a $0.8 \times 0.8 \times 3\ \text{mm}^3$ crystal [20]. This advanced result is due to the small dead space of tileable SiPMs and thin light guide used when compared with previous studies. High light collection leads to good energy performance.

The measured coincidence resolving time was 1.255 ns at the center of the crystal block. In the corner of the crystal block, we obtained better timing resolution than in the center possibly because the sum of the four position signals of the RCN was used for the extraction of timing information. In case of irradiation at the corner, the sum of the four position signals would be sharper than in the case of irradiation at the center because of the shorter signal pass and low equivalent resistance.

These results are comparable to the previous studies referred to above. However, it was reported that a SiPM has superior timing resolution (about 100 ps) for $LaBr_3$:Ce [5] and for LYSO (255 ps) [4]. In these studies, one-to-one coupling between a SiPM and the crystal and high bandwidth (over 1.8 GHz) amplifier with high gain (over $\times$ 50) yielded better performance. For this reason we expect

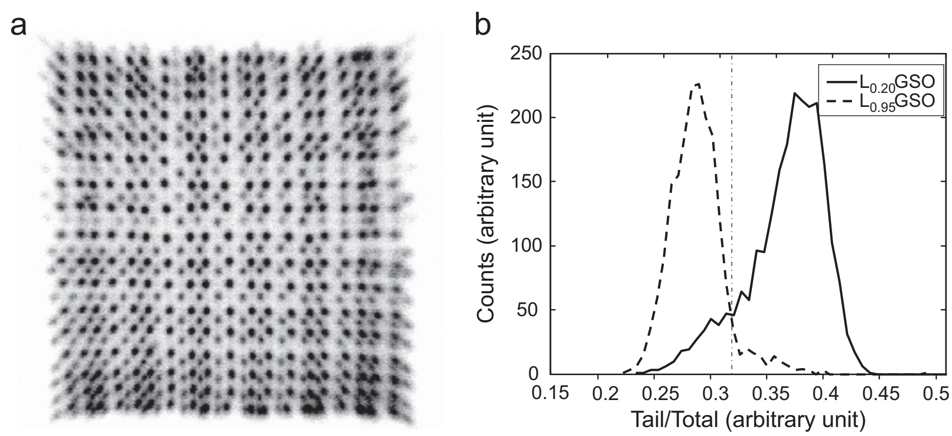

Fig. 7. Experimental result from the dual-layer DOI detector. (a) Flood map of both upper (19×17) and lower (20×18) layers using the relative offset method. (b) Tail integration to full integration ratio of $L_{0.95}GSO$ (dash line) and $L_{0.2}GSO$ (solid line). The dot-and-dash line indicates the threshold.

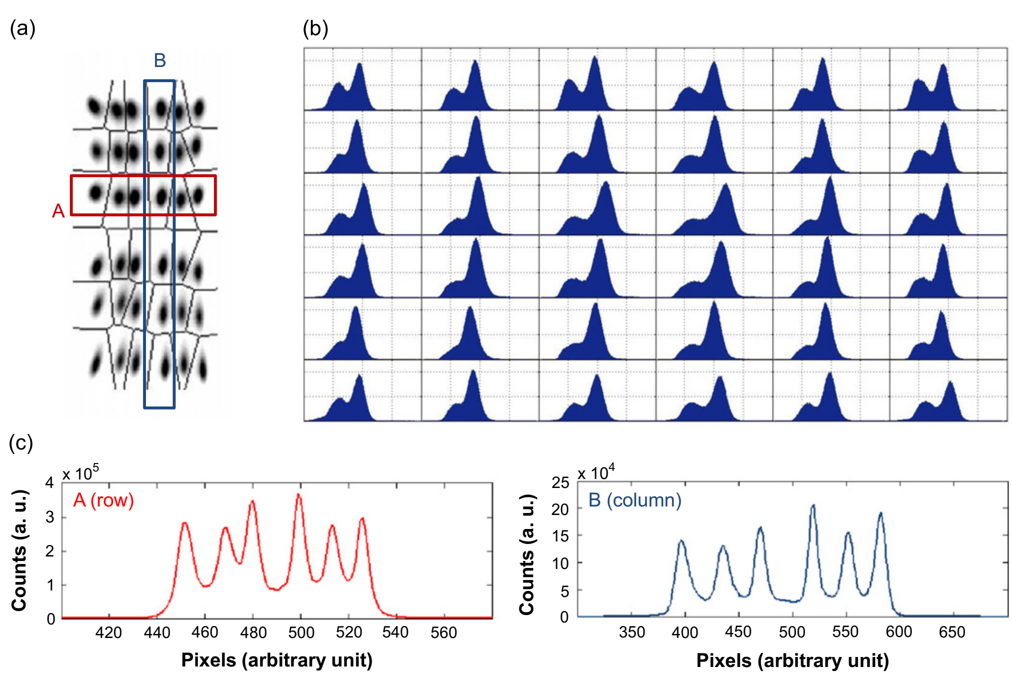

Fig. 8. Crystal map and energy spectra of the short optical fiber PET block detector. The 6×6 crystal was well separated in the crystal map and the energy resolution was $25.6 \pm 1.11\%$. (a) Flood map. (b) Energy spectra. (c) Profiles.

that the timing resolution can be improved further using higher bandwidth differential amplifiers than those used in this study (350 MHz).

This detector was also suitable for a double-layer DOI detector and short optical fiber PET detector. The energy resolution of short optical fiber PET was somewhat degraded because the light was lost through the optical fiber. Although the size of each SiPM channel (3×3 mm) is much larger than the distance between the crystal centers ($\sim$0.8 mm), all the crystals were well distinguished in the relative offset method for DOI encoding.

The results of this study indicate that several PET block detectors developed using a multi-purpose readout module and tileable multichannel SiPMs have suitable spatial resolution, energy and timing performance for small animal imaging when compared with commercially available PET devices. However, it should be noted that the current readout module employs the charge division network for signal multiplexing, which is vulnerable to the pulse pileup error in high count rate conditions. Therefore applying subsequent methods for reducing the pulse pileup error is advisable to obtain better count rate performances.

Acknowledgments

This work was supported by grants from the Atomic Energy R&D Program (2008–2003852, 2010-0026012) and the WCU Program (R31-10089) through the KOSEF funded by the Korean Ministry of Education, Science, and Technology.

References

[1] D. Renker, E. Lorenz, Journal of Instrumentation 4 (2009) 04004.
[2] J.S. Lee, S.J. Hong, in: K. Iniewski (Ed.), Electronic Circuits for Radiation Detection, CRC Press, FL (USA), 2010, pp. 179–200.
[3] E. Roncali, S.R. Cherry, Annals of Biomedical Engineering 39 (2011) 1358.
[4] C.L. Kim, D.L. McDaniel, A. Ganin, IEEE Transactions on Nuclear Science 58 (2011) 3.
[5] D.R. Schaart, S. Seifert, R. Vinke, H.T. van Dam, P. Dendooven, H. Lohner, F.J. Beekman, Physics in Medicine and Biology 55 (2010) N179.
[6] R. Vinke, H. Lohner, D.R. Schaart, H.T. van Dam, S. Seifert, F.J. Beekman, P. Dendooven, Nuclear Instruments and Methods in Physics Research Section A 610 (2009) 188.
[7] S.J. Hong, I.C. Song, M. Ito, S.I. Kwon, G.S. Lee, K.S. Sim, K.S. Park, J.T. Rhee, J.S. Lee, IEEE Transactions on Nuclear Science 55 (2008) 882.
[8] S.J. Hong, C.M. Kim, S.M. Cho, H. Woo, G.B. Ko, S.I. Kwon, J.T. Rhee, I.C. Song, J.S. Lee, IEEE Transactions on Nuclear Science 58 (2011) 579.
[9] S. Yamamoto, M. Imaizumi, Y. Kanai, M. Tatsumi, M. Aoki, E. Sugiyama, M. Kawakami, E. Shimosegawa, J. Hatazawa, Annals of Nuclear Medicine 24 (2010) 89.
[10] H.S. Yoon, G.B. Ko, S. Il Kwon, C.M. Lee, M. Ito, I.C. Song, D.S. Lee, S.J. Hong, J.S. Lee, Journal of Nuclear Medicine 53 (2012) 608.
[11] S.J. Hong, H.G. Kang, G.B. Ko, I.C. Song, J.T. Rhee, J.S. Lee, Physics in Medicine and Biology 57 (2012) 3869.
[12] V. Schulz, B. Weissler, P. Gebhardt, T. Solf, C.W. Lerche, P. Fischer, M. Ritzert, V. Mlotok, C. Piemonte, B. Goldschmidt, SiPM based preclinical PET/MR insert for a human 3 T MR: first imaging experiments, in: Proceedings of the IEEE NSS/MIC Conference Record, 2011, p. 4467.
[13] A. Kolb, E. Lorenz, M.S. Judenhofer, D. Renker, K. Lankes, B.J. Pichler, Physics in Medicine and Biology 55 (2010) 1815.
[14] V. Spanoudaki, A. Mann, A. Otte, I. Konorov, I. Torres-Espallardo, S. Paul, S. Ziegler, Journal of Instrumentation 2 (2007) P12002.
[15] J.S. Lee, Open Nuclear Medicine Journal 2 (2010) 192.
[16] S.I. Kwon, J.S. Lee, H.S. Yoon, M. Ito, G.B. Ko, J.Y. Choi, S.H. Lee, I.C. Song, J.M. Jeong, D.S. Lee, S.J. Hong, Journal of Nuclear Medicine 52 (2011) 572.
[17] D.R. Schaart, H.T. van Dam, S. Seifert, R. Vinke, P. Dendooven, H. Lohner, F.J. Beekman, Physics in Medicine and Biology 54 (2009) 3501.
[18] F. Taghibakhsh, A. Reznik, J.A. Rowlands, Nuclear Instruments and Methods in Physics Research Section A 633 (2011) S250.
[19] S. Moehrs, A. Del Guerra, D.J. Herbert, M.A. Mandelkern, Physics in Medicine and Biology 51 (2006) 1113.
[20] T.Y. Song, H.Y. Wu, S. Komarov, S.B. Siegel, Y.C. Tai, Physics in Medicine and Biology 55 (2010) 2573.
[21] J.S. Lee, M. Ito, K.S. Sim, B. Hong, K.S. Lee, J. Muhammad, J.T. Rhee, G.S. Lee, K.S. Park, I.C. Song, Journal of Korean Physical Society 50 (2007) 1332.
[22] S. Siegel, R.W. Silverman, Y.P. Shao, S.R. Cherry, IEEE Transactions on Nuclear Science 43 (1996) 1634–1641.
[23] F. Corsi, A. Dragone, C. Marzocca, A. Del Guerra, P. Delizia, N. Dinu, C. Piemonte, M. Boscardin, G.F.Dalla Betta, Nuclear Instruments and Methods in Physics Research Section A 572 (2007) 416.
[24] K. Yamamoto, K. Yamamura, K. Sato, S. Kamakura, S. Ohsuka, Nuclear Instruments and Methods in Physics Research Section A 636 (2011) S214.
[25] G.B. Ko, H.S. Yoon, S.I. Kwon, S.J. Hong, D.S. Lee, J.S. Lee, Biomedical Engineering Letters 1 (2011) 27–31.
[26] J.P. Lee, M. Ito, J.S. Lee, Biomedical Engineering Letters 1 (2011) 174.
[27] H. Liu, T. Omura, M. Watanabe, T. Yamashita, Nuclear Instruments and Methods in Physics Research Section A 459 (2001) 182–190.
[28] N. Zhang, C.J. Thompson, F. Cayouette, D. Jolly, S. Kecani, IEEE Transactions on Nuclear Science 50 (2003) 1624.
[29] J. Seidel, J.J. Vaquero, S. Siegel, W.R. Gandler, M.V. Green, IEEE Transactions on Nuclear Science 46 (1999) 485.
[30] H.S. Yoon, J.S. Lee, S.I. Kwon, M. Ito, K.-S. Sim, G.S. Lee, J.T. Rhee, S.J. Hong, Journal of Nuclear Medicine Meeting Abstracts 50 (2009) 296.